

Electron-hole and plasmon excitations in 3d transition metals: *Ab initio* calculations and inelastic x-ray scattering measurements

I. G. Gurtubay¹, J. M. Pitarke^{1,2}, Wei Ku³, A. G. Eguiluz^{4,5},
B. C. Larson⁵, J. Tischler⁵, P. Zschack⁶, and K. D. Finkelstein⁷

¹*Materia Kondentsatuaren Fisika Saila, Zientzi Fakultatea, Euskal Herriko Unibertsitatea, 644 Posta kutxatila, E-48080 Bilbo, Basque Country, Spain*

²*Donostia International Physics Center (DIPC) and Unidad de Física Materiales CSIC-UPV/EHU, Manuel de Lardizabal Pasealekua, E-20018 Donostia, Basque Country, Spain*

³*Department of Physics, Brookhaven National Laboratory, Bldg 510, Upton, NY 11973-5000 and Department of Physics and Astronomy, SUNY Stony Brook, Stony Brook, New York 11794-3800*

⁴*Department of Physics and Astronomy, The University of Tennessee, Knoxville, Tennessee 37996-1200*

⁵*Condensed Matter Sciences Division, Oak Ridge National Laboratory, Oak Ridge, Tennessee 37831-6030*

⁶*Frederick Seitz Materials Research Laboratory, University of Illinois, Urbana-Champaign, Illinois 61801*

⁷*CHESS, Cornell University, Ithaca, NY 14853*

(Dated: October 28, 2018)

We report extensive all-electron time-dependent density-functional calculations and nonresonant inelastic x-ray scattering measurements of the dynamical structure factor of 3d transition metals. For small wave vectors, a plasmon peak is observed which is well described by our calculations. At large wave vectors, both theory and experiment exhibit characteristic low-energy electron-hole excitations of *d* character which correlate with the presence of *d* bands below and above the Fermi level. Our calculations, which have been carried out in the random-phase and adiabatic local-density approximations, are found to be in remarkable agreement with the measured dynamical structure factor of Sc and Cr at energies below the semicore onset energy (M-edge) of these materials.

PACS numbers: 78.70.Ck, 71.15.Mb, 71.45.Gm

I. INTRODUCTION

Electron-hole and plasmon excitations in solids have been investigated for many years on the basis of the wave-vector and frequency dependent dynamical electron density response of the solid.¹ The first theoretical investigations of the dynamical density response function which take into account explicitly the band structure of the solid were performed during the last decade.^{2,3,4} Since then, first-principles calculations of the dynamical response of real solids have been reported for simple metals and semiconductors,^{5,6,7} and also for the noble metals Cu,⁸ Ag,⁹ and Au,¹⁰ a few transition metals,^{11,12} the transition-metal oxides TiO₂^{13,14} and NiO,¹⁵ MgB₂,¹⁶ and manganites.¹⁷ Most of these calculations discuss the response of the solid in the framework of time-dependent density functional theory (TDDFT) within the random-phase approximation (RPA) and also incorporating the many-body effects, i.e. exchange and correlation effects, using some local-density approximation (LDA). In general, these approximations have proven to be quite effective when studying excitations which do not involve localized states.

Vast *et al.*¹³ have recently reported *ab initio* calculations of the electron energy-loss spectrum of the transition metal oxide TiO₂, focusing on the excitation from the Ti 3p semicore levels. They have compared their results with electron energy-loss spectroscopy (EELS) measurements and have found that the inclusion of crystal local-field effects (CLFE), which arise when the microscopic electric field varies rapidly over the unit cell,¹⁸

turns out to be crucial for a faithful description of the experimental spectrum for small wave vectors.

The dynamical electron density response of solids can be probed with the use of optical absorption experiments,¹⁹ EELS,^{19,20} and inelastic x-ray scattering (IXS) techniques.²¹ In particular, the advent of synchrotron sources and high-resolution IXS facilities have allowed detailed investigations of the processes responsible for short-range many-body effects at large wave vectors.^{22,23,24} Macrander *et al.*²⁵ have reported the first IXS measurements showing a strong spectral peak for excitations from Ti 3p semicore states to empty states above the Fermi level. In particular, these authors measured the dynamical structure factor for Ti and TiC single crystals for intermediate and large momentum transfers, and in the case of TiC they compared their measurements to local-density-functional calculations with no inclusion of crystal local-field effects. Montano *et al.*²⁶ included these effects in the study of the dynamical structure factor of SiC for large wave vectors, finding the inclusion of crystal local-field effects to be very important in order to explain the measured IXS spectrum. More recently, Gurtubay *et al.*¹⁴ have found that large crystal local-field effects in the dynamical structure factor of TiO₂ yield a sharp loss peak in the low-energy regime (~ 14 eV), which is also present in the experimental IXS spectra.

In this paper, we report extensive all-electron TDDFT calculations and nonresonant IXS measurements of the dynamical structure factor of various 3d transition metals with *d* states below and above the Fermi level. For

small wave vectors, a plasmon peak is observed which is well described by our calculations. At large wave vectors, both theory and experiment exhibit a sharp peak which is absent for small wave vectors and which we argue to be originated in the presence of direct d -to- d transitions involving d states below and above the Fermi level. Comparison between theory and experiment indicates that at low energies the basic physics of the dynamical response is contained in the random-phase approximation (RPA) as long as the crystal local-field effects are taken into account. Furthermore, our results indicate that the inclusion of many-body effects through an adiabatic LDA (ALDA) kernel yields an unexpectedly good description of the electronic response of valence electrons of predominant d character.

II. THEORY

A. Single-particle Bloch states: LAPW basis

The starting point of our calculations is a set of well-converged Bloch states $\phi_{\mathbf{k},n}$ and energies $\varepsilon_{\mathbf{k},n}$, which are the eigenfunctions and eigenvalues of the Kohn-Sham equation of density-functional theory (DFT).^{27,28} For an accurate description of the dynamics of transition metals with narrow d bands, we expand these Bloch states in a linearized augmented plane wave (LAPW) basis,^{29,30} as follows

$$\phi_{\mathbf{k},n}(\mathbf{r}) = \sum_{\mathbf{G}} C_{\mathbf{k},n}(\mathbf{G}) \psi_{\mathbf{k}+\mathbf{G}}^{\text{LAPW}}(\mathbf{r}), \quad (1)$$

\mathbf{G} being vectors of the reciprocal lattice.

The choice of the basis functions $\psi_{\mathbf{k}+\mathbf{G}}^{\text{LAPW}}(\mathbf{r})$ is made by partitioning the primitive unit cell into non-overlapping muffin-tin spheres centered on the atomic nuclei, where the electronic environment retains an atomic-like nature, and the interstitial region, where electrons may be described by plane waves. The full effective potential entering the Kohn-Sham equation of DFT is expressed accordingly, i.e., it is expanded in lattice harmonics inside the atomic spheres and it is described by using a Fourier series in the interstitials. The maximum reciprocal-lattice vector \mathbf{G}_{max} that we consider in the expansion of Eq. (1) will be dictated by the cut-off parameter $R_{MT} \times G_{max}$, R_{MT} being the radius of the smallest muffin-tin sphere in the unit cell.

B. Kohn-Sham density-response function

Once we have an accurate description of the Kohn-Sham single-particle Bloch states $\phi_{\mathbf{k},n}$ and energies $\varepsilon_{\mathbf{k},n}$, we evaluate the density-response function $\chi^0(\mathbf{r}, \mathbf{r}', \omega)$ of noninteracting electrons moving in the effective Kohn-Sham potential of DFT.⁴¹ Since this quantity must keep

the periodicity of the solid, one can write

$$\chi^0(\mathbf{r}, \mathbf{r}', \omega) = \frac{1}{\Omega} \sum_{\mathbf{k}} \sum_{\mathbf{G}, \mathbf{G}'} e^{i(\mathbf{k}+\mathbf{G})\cdot\mathbf{r}} e^{-i(\mathbf{k}+\mathbf{G}')\cdot\mathbf{r}'} \chi_{\mathbf{G}, \mathbf{G}'}^0(\mathbf{k}, \omega), \quad (2)$$

where \mathbf{k} is a vector in the first Brillouin zone (BZ) and the Fourier coefficients $\chi_{\mathbf{G}, \mathbf{G}'}^0(\mathbf{k}, \omega)$ are given by the following expression:

$$\chi_{\mathbf{G}, \mathbf{G}'}^0(\mathbf{k}, \omega) = \frac{1}{\Omega} \sum_{\mathbf{k}'} \sum_{n, n'} \frac{f_{\mathbf{k}',n} - f_{\mathbf{k}'+\mathbf{k},n'}}{\varepsilon_{\mathbf{k}',n} - \varepsilon_{\mathbf{k}'+\mathbf{k},n'} + \hbar(\omega + i\eta)} \times \langle \phi_{\mathbf{k}',n} | e^{-i(\mathbf{k}+\mathbf{G})\cdot\mathbf{r}} | \phi_{\mathbf{k}'+\mathbf{k},n'} \rangle \langle \phi_{\mathbf{k}'+\mathbf{k},n'} | e^{i(\mathbf{k}+\mathbf{G}')\cdot\mathbf{r}} | \phi_{\mathbf{k}',n} \rangle. \quad (3)$$

Here, Ω represents the normalization volume, η is a positive infinitesimal, and $f_{\mathbf{k},n}$ are Fermi factors, which at zero temperature ($T = 0$) are simply given by the Heaviside step function

$$f_{\mathbf{k},n} = 2 \Theta(\varepsilon_F - \varepsilon_{\mathbf{k},n}), \quad (4)$$

ε_F being the Fermi energy of the solid.

The major task in the calculation of the Fourier coefficients $\chi_{\mathbf{G}, \mathbf{G}'}^0(\mathbf{k}, \omega)$ resides in the computation of the matrix elements entering Eq. (3). Using Eq. (1), both the integration over angular variables and the sum over reciprocal-lattice vectors can be done analytically, and one finds explicit expressions for the matrix elements in terms of one-dimensional integrals involving basis radial functions and spherical Bessel functions.³¹

C. Interacting density-response function

In the framework of TDDFT,^{32,33,34} the *exact* density-response function $\chi(\mathbf{r}, \mathbf{r}', \omega)$ of a periodic solid of electron density $n_0(\mathbf{r})$ can be expanded in a Fourier series of the form of Eq. (2), with the Fourier coefficients $\chi_{\mathbf{G}, \mathbf{G}'}(\mathbf{k}, \omega)$ given by the following expression:

$$\chi_{\mathbf{G}, \mathbf{G}'}(\mathbf{k}, \omega) = \chi_{\mathbf{G}, \mathbf{G}'}^0(\mathbf{k}, \omega) + \sum_{\mathbf{G}_1, \mathbf{G}_2} \chi_{\mathbf{G}, \mathbf{G}_1}^0(\mathbf{k}, \omega) \times \{ v_{\mathbf{G}_1}(\mathbf{k}) \delta_{\mathbf{G}_1, \mathbf{G}_2} + f_{\mathbf{G}_1, \mathbf{G}_2}^{\text{XC}}[n_0](\mathbf{k}, \omega) \} \chi_{\mathbf{G}_2, \mathbf{G}'}(\mathbf{k}, \omega), \quad (5)$$

where $\chi_{\mathbf{G}, \mathbf{G}'}^0(\mathbf{k}, \omega)$ are the Fourier coefficients of Eq. (3), $v_{\mathbf{G}}(\mathbf{k}) = 4\pi e^2 / |\mathbf{k} + \mathbf{G}|^2$ is the Fourier transform of the bare Coulomb potential, and $f_{\mathbf{G}, \mathbf{G}'}^{\text{XC}}[n](\mathbf{k}, \omega)$ are the Fourier coefficients of the functional derivative of the time-dependent exchange-correlation (XC) potential of TDDFT. In the RPA, the XC kernel $f_{\mathbf{G}, \mathbf{G}'}^{\text{XC}}[n](\mathbf{k}, \omega)$ is taken to be zero; in the ALDA, it is approximated by an adiabatic kernel of the form

$$f_{\mathbf{G}, \mathbf{G}'}^{\text{XC}}(\mathbf{k}, \omega) = \int d\mathbf{r} e^{-i(\mathbf{G}-\mathbf{G}')\cdot\mathbf{r}} \left. \frac{dV_{\text{XC}}(n)}{dn} \right|_{n=n_0(\mathbf{r})}, \quad (6)$$

where $V_{\text{XC}}(n)$ is the XC potential of a homogeneous electron gas of density n .

D. Dynamical structure factor and x-ray inelastic scattering cross section

The dynamical structure factor $S(\mathbf{q}, \omega)$ of a many-electron system, which determines the electron-density fluctuations at a given wave vector \mathbf{q} and frequency ω , is connected to the imaginary part of the density-response function $\chi(\mathbf{r}, \mathbf{r}', \omega)$ through the fluctuation-dissipation theorem.³⁵ In the case of a periodic solid at $T = 0$, one finds

$$S(\mathbf{k} + \mathbf{G}, \omega) = -2 \hbar \Omega \text{Im} \chi_{\mathbf{G}, \mathbf{G}}(\mathbf{k}, \omega), \quad (7)$$

\mathbf{k} being a wave vector in the first BZ.

Within the first-Born approximation, the double differential scattering cross-section for x rays to transfer momentum $\hbar(\mathbf{k} + \mathbf{G})$ and energy $\hbar\omega$ to a periodic solid is given by

$$\frac{d^2\sigma}{d\Omega d\omega} = \left(\frac{e^2}{m_e c^2} \right)^2 (\mathbf{e}_i \cdot \mathbf{e}_f)^2 \left(\frac{\omega_f}{\omega_i} \right) S(\mathbf{k} + \mathbf{G}, \omega), \quad (8)$$

where $(\mathbf{e}_i, \mathbf{e}_f)$ and (ω_i, ω_f) refer to the polarization vector and frequency of the incident and scattered photon, respectively.

E. Dielectric matrix and macroscopic dielectric function

In order to investigate the contribution to the energy-loss spectrum coming from the excitation of plasmons, it is convenient to consider the wave-vector and frequency dependent inverse dielectric matrix of a periodic solid which yields the potential induced at a given point of space by an arbitrary (small) frequency-dependent external potential. One finds

$$\epsilon_{\mathbf{G}, \mathbf{G}'}^{-1}(\mathbf{k}, \omega) = \delta_{\mathbf{G}, \mathbf{G}'} + v_{\mathbf{G}}(\mathbf{k}) \chi_{\mathbf{G}, \mathbf{G}'}(\mathbf{k}, \omega), \quad (9)$$

with \mathbf{k} being a vector in the first Brillouin zone.

For \mathbf{k} wave vectors in the first Brillouin zone, the macroscopic dielectric function is defined as follows

$$\epsilon_M(\mathbf{k}, \omega) = 1/\epsilon_{0,0}^{-1}(\mathbf{k}, \omega), \quad (10)$$

where $\epsilon_{0,0}^{-1}(\mathbf{k}, \omega)$ represents the first diagonal element of the inverse dielectric matrix of Eq. (9). In the absence of crystal local-field effects (CLFE), the off-diagonal elements of the inverse dielectric matrix are negligible and the macroscopic dielectric function coincides, therefore, with the first diagonal element of the dielectric matrix, $\epsilon_{\mathbf{G}, \mathbf{G}}(\mathbf{k}, \omega)$, which in the RPA is given by the following expression:

$$\epsilon_{\mathbf{G}, \mathbf{G}'}^{RPA}(\mathbf{k}, \omega) = \delta_{\mathbf{G}, \mathbf{G}'} - v_{\mathbf{G}}(\mathbf{k}) \chi_{\mathbf{G}, \mathbf{G}'}^0(\mathbf{k}, \omega). \quad (11)$$

Collective excitations (plasmons) are known to occur at energies where both the real and the imaginary part of

the macroscopic dielectric function are close to zero. On the other hand, the diagonal elements of the imaginary part of the RPA dielectric matrix are known to represent a measure of the number of states available for real transitions involving a given momentum transfer $\hbar\mathbf{q}$ and energy transfer $\hbar\omega$.

III. EXPERIMENT

Nonresonant inelastic x-ray scattering measurements of the dynamical structure factor $S(\mathbf{q}, \omega)$ of single crystals Sc and Cr have been obtained using the UNICAT undulator Beam Line on the Advanced Photon Source (APS) at Argonne National Laboratory. The measurements were made in symmetric reflection geometry, with 7.6 keV x-rays, a range of wave vectors from 0.5 to 3.98 \AA^{-1} , and an energy resolution of 1.1 eV. The shape-asymmetry of the tails of the quasi-elastic scattering near zero energy transfer for the analyzer and scattering geometry used was determined directly by measurements made on wide band-gap (> 10 eV) insulators (e.g. LiF, CaF₂), which indicated the tails to be symmetric for losses greater than 2.5 eV. The quasi-elastic contribution to the scattering for Sc and Cr was then removed using measurements on the energy gain side of the quasi-elastic peak and restricting the data to energy losses of 2.5 eV or greater. The rapid falloff of the quasi-elastic contribution rendered the tails insignificant for energy losses greater than 6-8 eV for the conditions used.

In order to reduce to absolute units the APS spectra of the transition metals Sc and Cr, we have first performed an absolute measurement on Al.³⁶ For measurements that do not extend past the Al L-edge at ~ 72 eV, only the three valence electrons of this metal contribute to the first-moment f sum-rule

$$\int_0^{\omega_{max}} d\omega \omega s(\mathbf{q}, \omega) = \alpha \frac{n_0 \pi}{m_e} q^2. \quad (12)$$

Here, n_0 is the average electron density of the $3s^2 3p^1$ valence electrons in Al, and $s(\mathbf{q}, \omega)$ is the reduced dynamical structure factor: $s(\mathbf{q}, \omega) = S(\mathbf{q}, \omega)/(\hbar\Omega)$. According to Eq. (8), the dynamical structure factor should be proportional to the relative intensity $I(\mathbf{q}, \omega)/I_0$ of the scattered beam, I_0 being the incident beam power; hence,

$$s(\mathbf{q}, \omega) = C I(\mathbf{q}, \omega)/I_0. \quad (13)$$

The maximum energy $\hbar\omega_{max}$ entering the left-hand side of Eq. (12) must be below the 72 eV semicore onset energy and the coefficient α represents the relative contribution of valence $3s^2 3p^1$ electrons to the f sum-rule for energies below $\hbar\omega_{max}$. We have carried out *ab initio* pseudopotential calculations of the dynamical structure factor of Al, and for $\hbar\omega_{max} = 65$ eV we have found $\alpha = 0.95$.

Introducing Eq. (13) into Eq. (12) one finds the calibration factor C , which we have derived from our IXS

measurements of the $I(\mathbf{q}, \omega)/I_0$ ratio in an Al sample. (See Ref. 36 for details.) Since this calibration factor is inversely proportional to the effective volume of material sampled by the x-ray beam (and is independent of the atomic configuration of the material) and for thick samples and symmetric Bragg geometry the volume ratio of the material sampled in different targets is given by the ratio of the corresponding linear absorption coefficients, the dynamical structure factor $s_X(\mathbf{q}, \omega)$ of an arbitrary (X) target can be obtained from the following expression:

$$s_X(\mathbf{q}, \omega) = C \mu_X / \mu_{Al} I_X(\mathbf{q}, \omega) / I_0, \quad (14)$$

with μ_X and μ_{Al} being the linear absorption coefficients of the X material and Al, respectively.

As suggested in Ref. 36, analogous (albeit sample geometry and \mathbf{q} -dependent) expressions for the ratio of the effective scattering volumes can be derived for transmission geometry and non-symmetric reflection scattering geometry.

IV. RESULTS AND DISCUSSION

In this section, we first present TDDFT calculations and nonresonant IXS measurements of the dynamical structure factor of the hexagonal close-packed (hcp) Sc and the body-centered cubic (bcc) Cr. Then, we present a comparison of the dynamical response of the transition metals Sc, Ti, V, Cr, Fe, Co, and Ni, all belonging to the $3d$ series, and we focus on the evolution of a low-energy peak that is visible at large wave vectors and which is originated in the presence of d -to- d transitions involving d -states below and above the Fermi level.

All the calculations presented below have been carried out by first expanding Bloch states in an LAPW basis, as in Eq. (1), with a cutoff parameter of $R_{MT} \times G_{max} = 8$, using spherical harmonics inside the atomic spheres up to $l = 10$, and including $3s$ and $3p$ states as semicore states. We have then solved self-consistently the Kohn-Sham equation of DFT in the local-density approximation (LDA), with use of the Perdew-Wang parametrization³⁷ of the Ceperley-Alder XC energy of a uniform electron gas,³⁸ we have calculated the Fourier coefficients $\chi_{\mathbf{G}, \mathbf{G}}^0(\mathbf{k}, \omega)$ from Eq. (3) by keeping unoccupied KS states up to 7.5 Ry, and we have finally solved Eq. (5) either in the RPA or the ALDA with a finite damping parameter $\eta = 0.65$ eV.

In the case of the hexagonal close-packed Sc, Ti, and Co, the coefficients $\chi_{\mathbf{G}, \mathbf{G}}(\mathbf{k}, \omega)$ have been evaluated for wave vectors perpendicular to the hexagonal plane, i.e., along the (001) direction, and well-converged results have been obtained by using a $8 \times 8 \times 16$ sampling of the BZ corresponding to 90 points in the irreducible BZ (IBZ). In the case of the body-centered cubic Cr, V, and Fe, calculations have been performed for wave vectors along the (100), (110), and (111) directions, and well-converged results have been obtained by using a $10 \times 10 \times 10$ sampling of the BZ corresponding to 47 points in the IBZ. Finally,

for the face-centered cubic Ni the coefficients $\chi_{\mathbf{G}, \mathbf{G}}(\mathbf{k}, \omega)$ have been evaluated for wave vectors along the (100) direction, and well-converged results have been obtained by using a $12 \times 12 \times 12$ sampling of the BZ corresponding to 72 points in the IBZ.

In order to investigate the impact of crystal local-field effects, we have first neglected these effects by considering only the diagonal elements of the Kohn-Sham density-response matrix entering Eq. (5) (diagonal calculation), and we have then solved the matrix equation with a given number of \mathbf{G} vectors (full calculation). Well-converged results have been obtained with the use of 35, 43 and 51 \mathbf{G} vectors in hcp, bcc and fcc structures, respectively.⁴²

A. Sc

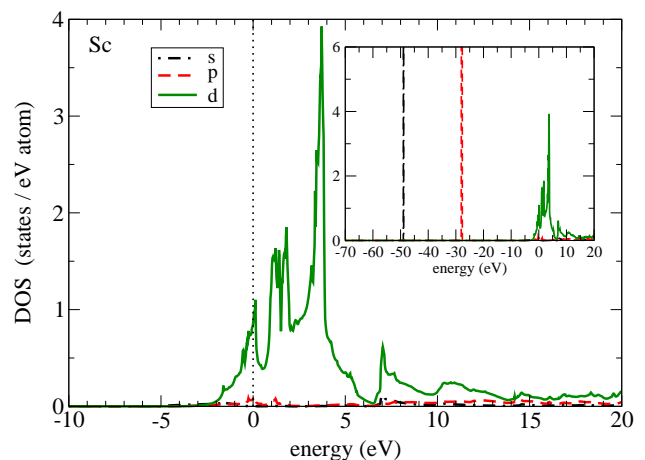


FIG. 1: (Color online) Density of states (DOS) of Sc, at energies near the Fermi level (dotted line) for each component of the angular momentum inside the atomic sphere. Dash-dotted black, dashed red and solid green lines denote the number of states per atom and per eV with s , p , and d character, respectively. The inset shows a wider energy range, in which the $3s$ (dash-dotted black line) and $3p$ (dashed red line) semicore states can be distinguished.

Sc ($[Ar] 3d^1 4s^2$) being the first of the transition metals has a single $3d$ electron per atom. Hence, the $3d$ band is located below and above the Fermi level, as shown by the density of states (DOS) drawn by a solid green curve in Fig. 1. The inset of this figure shows the location of the $3s^2$ (dash-dotted black line) and $3p^6$ (dashed red line) semicore bands, which are located at ~ 49 eV and ~ 28 eV below the Fermi level, respectively.

Early measurements of the energy-loss spectra of high-energy electrons in Sc were reported by Brousseau-Lahaye *et al.* for small wave vectors.³⁹ A plasmon peak was identified at ~ 13 eV, which agrees with the expected plasmon energy of valence electrons ($3d^1 4s^2$) in Sc. Pseudopotential-based first-principles calculations of the energy-loss function of Sc were first reported by Schöne and Ekardt¹¹ at small and intermediate wave vec-

tors and more recently by Gurtubay *et al.*¹² A detailed analysis of the plasmon energy dispersion of this material was reported in Ref. 12, demonstrating that the plasmon peak at ~ 13 eV corresponds indeed to zero values of the real part of the macroscopic dielectric function where the imaginary part is small and showing that the crystal local-field effects have a considerable impact on the plasmon energy at small wave vectors which gives rise to an interplay with the XC effects built into the many-body kernel.

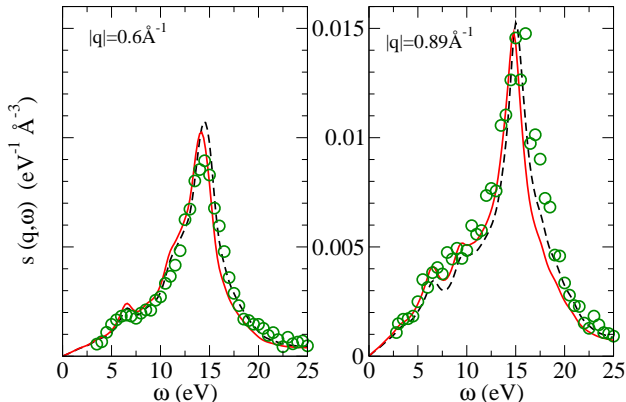


FIG. 2: (Color online) Reduced dynamical structure factor $s(\mathbf{q}, \omega) = S(\mathbf{q}, \omega)/(\hbar\Omega)$ of Sc, as obtained in the RPA (dashed black line), ALDA (solid red line), and by IXS measurements (green circles). The wave vector has been taken to be $\mathbf{q} = 8/16(001)$ (left panel) and $\mathbf{q} = 12/16(001)$ (right panel) in units of $2\pi/c$, c being the lattice constant in the z -direction.

In Fig. 2, we display new first-principles calculations (dashed black and solid red lines) and IXS measurements (green circles) of the dynamical structure factor $s(\mathbf{q}, \omega)$ of Sc at wave vectors of magnitude $|\mathbf{q}| = 0.6 \text{ \AA}^{-1}$ (left panel) and $|\mathbf{q}| = 0.89 \text{ \AA}^{-1}$ (right panel) and for energies below the ~ 28 eV semicore onset energy (M-edge) of this material. At these wave vectors, the dynamical structure factor displays a broad plasmon peak at ~ 15 eV, which corresponds roughly to the expected plasmon energy of three valence electrons per atom in Sc ($r_s = 2.38$);⁴³ nevertheless, the shape of this plasmon peak, which mixes with the fine structure caused by d -electron transitions, bears little resemblance to the plasmon peak of a homogeneous electron gas. In particular, some structure is present at energies between 5 and 10 eV; this structure, which is also present in the imaginary part of the dielectric matrix and has also been predicted to exist for smaller wave vectors,^{11,12} occurs in a region where interband transitions from the valence bands to unoccupied p states above the Fermi level take place.

Fig. 2 also shows that the agreement between our *ab initio* calculations and the experimental measurements is excellent, both in the energy of the plasmon and in the overall shape of the energy-loss spectrum. Furthermore, for energies below the plasmon peak the agreement between ALDA calculations (solid red line) and IXS mea-

surements is remarkable.

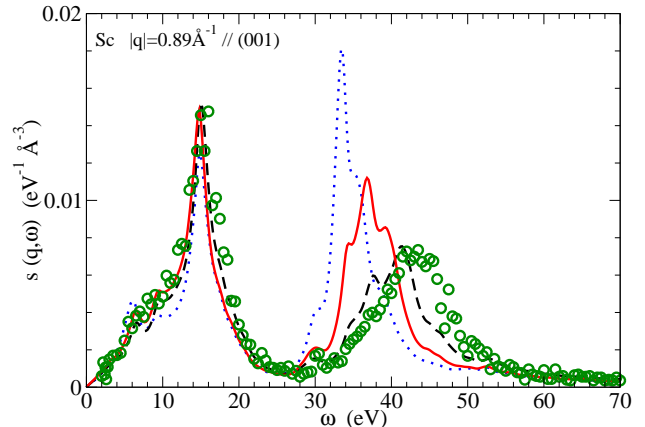


FIG. 3: (Color online) As in Fig. 2, but for $\mathbf{q} = 12/16(001)$ (in units of $2\pi/c$) and energies that include the excitation of $3p$ semicore states. The blue dotted line denotes the diagonal (i.e. without CLFE) RPA calculation.

First-principles calculations (dashed black and solid red lines) and IXS measurements (green circles) of the dynamical structure factor of Sc at $|\mathbf{q}| = 0.89 \text{ \AA}^{-1}$ are exhibited in Fig. 3 for energies up to 70 eV, well above the ~ 28 eV semicore onset energy (M-edge). For comparison, diagonal RPA calculations are also plotted in the same figure (blue dotted line), showing that the impact of crystal local-field effects is very large just above the M-edge, where transitions from the occupied Sc semicore $3p$ states to the lowest conduction bands occur. Crystal local-field effects bring the onset of the M-edge to larger energies and reduce the corresponding peak height, in close agreement with experiment. The shift to larger energies stems from the fact that the semicore states involved in these transitions are highly localized in real space and therefore neglecting the off-diagonal terms in Eq. (3), and subsequently in Eq. (9), underestimates the large dynamical screening effects near the semicore edge.

Figure 3 shows, however, that although our full RPA calculation (black dashed line) is in very good agreement with experiment (green circles) there is a mismatch between the ALDA calculation (red solid line) and the measured spectrum. This discrepancy calls for further investigations of (i) an improved description of single-particle energies beyond the LDA and (ii) accurate many-body kernels accounting for XC effects beyond the ALDA. Both RPA and ALDA calculations have been carried out with the very same form of the XC potential entering the KS equation of DFT. Hence, we can rule out our approximate XC potential as the origin of the *large* discrepancy between ALDA calculations and experiment, and sources of error of our ALDA calculations should be searched both in the adiabaticity and the locality of the ALDA XC kernel in a solid where inhomogeneities of both the static unperturbed electron density and the induced density play an important role, especially when

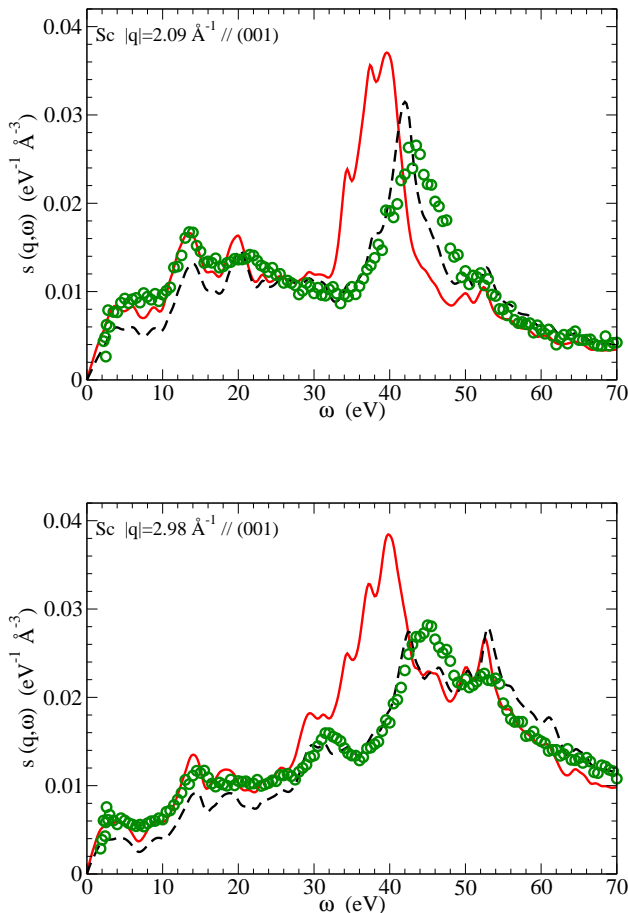


FIG. 4: (Color online) Dynamical structure factor $s(\mathbf{q}, \omega)$ of Sc, as obtained in the RPA (black dashed line), ALDA (red solid line), and by IXS measurements (green circles). The wave vector has been taken to be $\mathbf{q} = [4/16(001) + (002)]$ (upper panel) and $\mathbf{q} = [8/16(001) + (002)]$ (lower panel) in units of $2\pi/c$, c being the lattice constant in the z -direction.

semicore states with large binding energies are involved.

In Fig. 4, we show calculations and measurements of the dynamical structure factor of Sc, as in Fig. 2, but now at wave vectors of magnitude $|\mathbf{q}| = 2.09 \text{ \AA}^{-1}$ (upper panel) and $|\mathbf{q}| = 2.98 \text{ \AA}^{-1}$ (lower panel). At these large wave vectors, the plasmon energy falls into the electron-hole pair excitation continuum so there is no well-defined plasmon peak. Instead, a new feature appears in the dynamical structure factor at $\sim 4 \text{ eV}$, which is very sensitive to crystal local-field effects. A close examination of the various transitions that contribute to the KS density-response function of Eq. (3) indicates that this new feature, which is absent for small wave vectors, is originated in the presence of d -to- d transitions involving narrow d complexes lying below and above the Fermi level. Such direct d -to- d excitations have not been observed in optical absorption measurements (where the wave vector is zero) and EELS experiments (where the wave vector is small), which underscores the importance of IXS for the

examination of the electronic structure of these materials.

An inspection of Fig. 4 also shows that introducing many-body XC effects within the ALDA (red solid line) leads to a faithful description of the low-energy part of the measured energy-loss spectrum (green circles), as occurs for smaller wave vectors (see Figs. 2 and 3), even at $\sim 4 \text{ eV}$ where the energy loss is dictated by the presence of d -to- d transitions. At energies above the M-edge, the agreement between our full RPA calculations (black dashed line) and the IXS measurements is excellent, but there is a considerable mismatch between the ALDA calculation (red solid line) and the measured spectrum, as occurs for smaller wave vectors (see Fig. 3).

A closer look into the semicore energy region in Figs. 3 and 4 still shows a 2-3 eV mismatch between the calculated RPA and the measured IXS semicore excitation onset. This stems from a well-known deficiency of the local-density approximation we have used to describe our single-particle orbitals,⁴⁴ which in general underbinds the energy of highly localized occupied states and is known to occur even in the case of a simple metal such as Al.⁴⁵

B. Cr

Cr ($[Ar] 3d^5 4s^1$) lying in the middle of the $3d$ period exhibits a high density of both occupied and unoccupied d states near the Fermi level. Hence, this transition metal is the ideal candidate for the investigation of the characteristic d -to- d transitions that we have observed in the case of Sc.

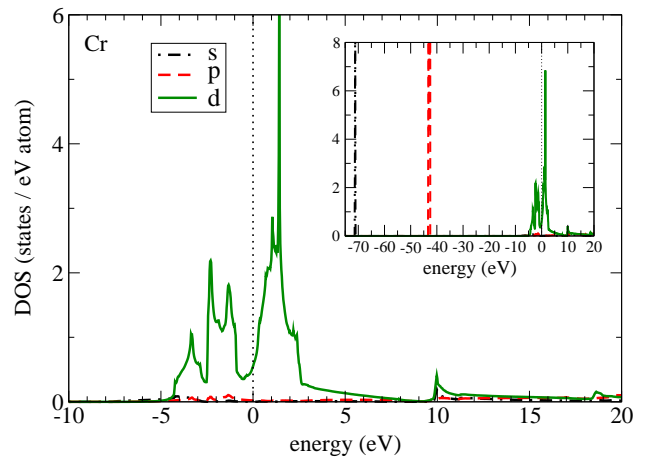


FIG. 5: (Color online) Density of states (DOS) of Cr near the Fermi level (dotted line) for each component of the angular momentum inside the atomic sphere. Black dash-dotted, red dashed, and green solid lines represent the number of states per atom and per eV of s , p , and d character, respectively. The inset shows a wider energy range, in which the $3s$ (black dash-dotted line) and $3p$ (red dashed line) semicore states are visible.

The density of states of Cr is depicted in Fig. 5, where

d states distributed at both sides of the Fermi level are represented by green solid lines. As in Fig. 1, the inset of this figure shows the location of the $3s$ (black dash-dotted line) and $3p$ (red dashed line) semicore states at ~ 70 eV and ~ 42 eV below the Fermi level, which hold 2 and 6 electrons per atom, respectively.

Inelastic x-ray scattering measurements of the energy-loss spectra of Cr were reported recently by Montano and Macrander⁴⁰ for momentum transfers ranging from 0.80 to 5.0 \AA^{-1} along the (110) direction. Spectral features were found corresponding to plasmon excitations, as well as a second peak corresponding to excitations from the $3p$ semicore states to the $3d$ valence states; however, no structure was visible at low energies near ~ 4 eV, where the x-ray spectrum was dominated by the quasielastic phonon scattering feature. To the best of our knowledge, no theoretical investigations of the dynamical response of this material have been reported before.

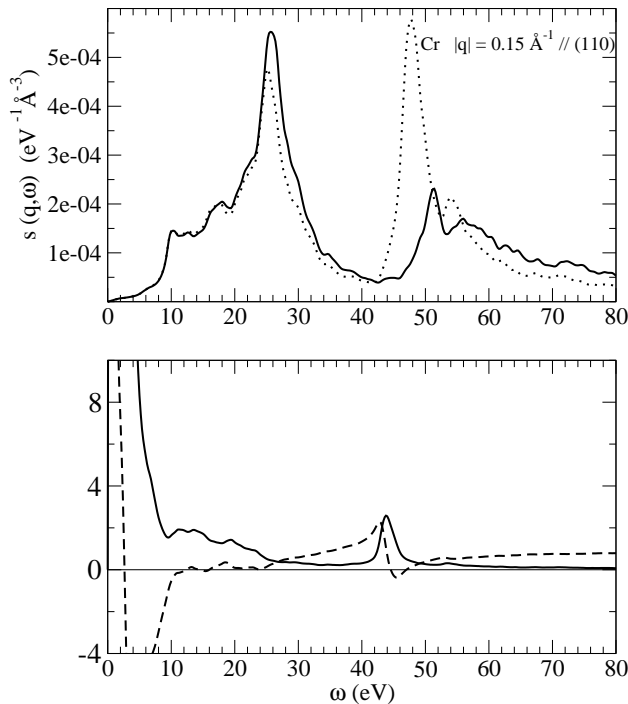


FIG. 6: Top panel: RPA full (solid line) and diagonal (dotted line) calculations of the dynamical structure factor $s(\mathbf{q}, \omega)$ of Cr. Bottom panel: RPA calculations of the real (dashed line) and imaginary (solid line) parts of the first diagonal element of the dielectric matrix $\epsilon_{\mathbf{G}, \mathbf{G}'}(\mathbf{q}, \omega)$ of Cr. In both panels, the wave vector has been taken to be $\mathbf{q} = 1/10(110)$ in units of $2\pi/a$, a being the lattice parameter.

The top panel of Fig. 6 shows first-principles RPA diagonal (dotted line) and full (solid line) calculations of the dynamical structure factor $s(\mathbf{q}, \omega)$ of Cr for small wave vectors of magnitude $|\mathbf{q}| = 0.15 \text{ \AA}^{-1}$ along the (110) direction. At energies below the ~ 43 eV semicore onset energy (M-edge), where crystal local-field effects are found to be small (diagonal and full calculations are very close from each other), we find a prominent broad feature at

~ 26 eV, which agrees with the expected plasmon energy of 6 valence electrons per atom in Cr ($r_s = 1.48$) and is clearly identifiable as a collective excitation of hybridized $3d^5$ and $4s^1$ valence electrons. Indeed, this peak corresponds (see the bottom panel of Fig. 6) to a zero value of the real part of the matrix element $\epsilon_{0,0}(\mathbf{q}, \omega)$ where $\text{Im}\epsilon_{0,0}(\mathbf{q}, \omega)$ is small.⁴⁶

At energies above the M-edge, transitions from the localized Cr semicore $3p$ states below the Fermi level to the lowest conduction bands take place. As a result, the impact of crystal local-field effects is large (see the top panel of Fig. 6), as occurs in the case of Sc. These effects bring the onset of the M-edge to larger energies and considerably reduce the peak height above the M-edge, which becomes a broad feature around 50-60 eV involving primarily excitations out of the $3p$ band of Cr.

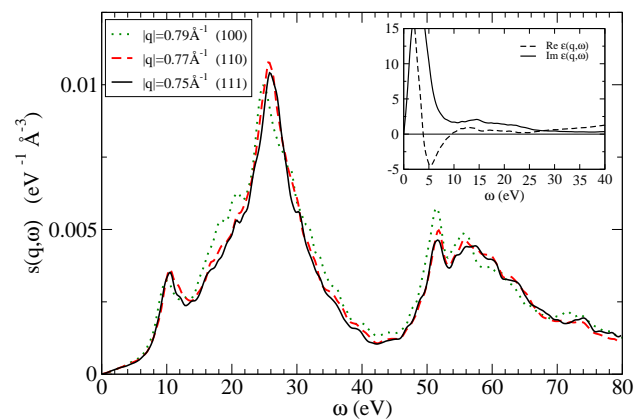


FIG. 7: (Color online) RPA calculations of the dynamical structure factor $s(\mathbf{q}, \omega)$ of Cr at wave vectors of magnitude $|\mathbf{q}| \approx 0.8 \text{ \AA}^{-1}$ along three high-symmetry directions. Dotted green, dashed red, and solid black lines correspond to $\mathbf{q} = 4/11(100)$, $\mathbf{q} = 5/20(110)$, and $\mathbf{q} = 2/10(111)$ wave vectors, respectively, in units of $2\pi/a$, a being the lattice parameter. The inset shows the real (dashed line) and imaginary (solid line) parts of the first diagonal element of the RPA dielectric matrix $\epsilon_{\mathbf{G}, \mathbf{G}'}(\mathbf{q}, \omega)$ at $|\mathbf{q}| = 0.75 \text{ \AA}^{-1}$.

In order to investigate the dependence of the dynamical structure factor of Cr on the direction of the wave vector, we have plotted in Fig. 7 the RPA dynamical structure factor $s(\mathbf{q}, \omega)$ of Cr at wave vectors of magnitude $|\mathbf{q}| \approx 0.8 \text{ \AA}^{-1}$ along the (100), (110), and (111) directions.⁴⁷ This figure shows that the dynamical structure factor of Cr is rather similar for all high-symmetry propagation directions. In particular, we note that the long-wavelength collective excitation at ~ 26 eV (see Fig. 6) is still visible along all propagation directions when the magnitude of the wave vector is $|\mathbf{q}| \approx 0.8 \text{ \AA}^{-1}$. This is in agreement with the IXS measurements reported by Montano and Macrander⁴⁰ for this magnitude of the wave vector along the (110) direction. Furthermore, that this feature is still originated in the building up of a collective excitation follows from the inset of Fig. 7, where the real and imaginary parts of the ma-

trix element $\epsilon_{0,0}(\mathbf{q}, \omega)$ are displayed: this feature corresponds to a zero value of $\text{Re}\epsilon_{0,0}(\mathbf{q}, \omega)$ (dashed line) where $\text{Im}\epsilon_{0,0}(\mathbf{q}, \omega)$ (solid line) is small. On the other hand, a comparison of the high-energy part of the energy-loss spectra of Figs. 6 and 7 indicates that the high-energy broad feature around 50-60 eV, which is also rather insensitive to the propagation direction and which involves primarily excitations out of the $3p$ band of Cr, has a considerable wave-vector dependence, becoming more pronounced as the wave vector increases.

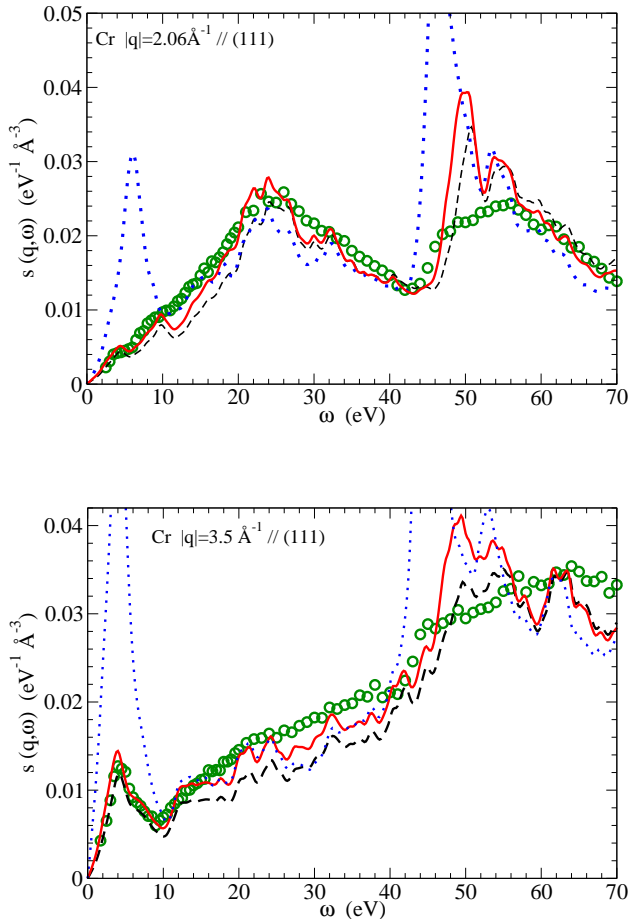


FIG. 8: (Color online) Dynamical structure factor of Cr (CLFE, i.e. off-diagonal terms in Eq.(9), included) along the (111) direction for wave vectors $\mathbf{q} = 6/11(001)$ (top panel) and $\mathbf{q} = 10/11(001)$ (bottom panel), within RPA (black dashed line) and ALDA (red solid line). The blue dotted line represents the calculation without CLFE and green circles, IXS measurements.

First-principles calculations and IXS measurements of the dynamical structure factor $s(\mathbf{q}, \omega)$ of Cr are displayed in Fig. 8 at large wave vectors of magnitude $|\mathbf{q}| = 2.06 \text{ \AA}^{-1}$ and $|\mathbf{q}| = 3.5 \text{ \AA}^{-1}$ along the (111) direction. As in the case of Sc, at these large wave vectors the prominent broad peak of Figs. 6 and 7 at ~ 26 eV, which is in the nature of collective excitations, is now replaced by a less pronounced broad feature at energies below the M-edge originated from single electron-hole ex-

citations, and the high-energy feature above the M-edge is found to gain weight as the wave vector increases.

For small wave vectors, crystal local-field effects only play a role at energies above the M-edge (see Figs. 6 and 7), where the energy-loss spectrum is dominated by transitions from very localized $3p$ bands below the Fermi level. The striking feature of Fig. 8 is precisely the fact that as the wave vector increases huge crystal local-field effects are present not only at energies above the M-edge but also at very low energies below 10 eV. In the absence of crystal local-field effects (blue dotted line), the energy loss spectra at the large wave vectors under consideration are clearly dominated by two distinct features at 4-6 eV and 40-60 eV. A close examination of the various transitions that contribute to the KS density-response function of Eq. (3) indicates that these features involve excitations to unoccupied d states above the Fermi level coming primarily from occupied d and p states, respectively. As in the case of Sc, high-energy transitions from occupied p states occur for arbitrary values of the wave vector; however, direct d -to- d transitions are not observed for small wave vectors. In the presence of crystal local-field effects (dashed black and solid red lines), both peak heights are considerably reduced and our calculated low-energy feature is brought into excellent agreement with experiment. Both theory and experiment exhibit the presence of a very well defined low-energy peak at ~ 4 eV, which is originated in the presence of direct d -to- d transitions and had never been observed before.

An inspection of Fig. 8 clearly indicates that (i) first-principles RPA calculations provide a reasonably good description of the measured low-energy peak at ~ 4 eV, provided that crystal local-field effects are included, (ii) inclusion of XC effects within the ALDA brings the low-energy peak at ~ 4 eV into excellent agreement with experiment, and (iii) the ALDA, which accurately accounts for XC effects at low energies even at large wave vectors, fails to give a quantitative description of the measured energy-loss spectra at energies above the M-edge. This suggests that for an accurate understanding of the energy-loss spectra of transition metals in the whole energy-range under study one should go beyond and adiabatic local-density approximation in the description of XC effects not present in the RPA. We also note that as in the case of Sc (see Figs. 3 and 4) both RPA (black dashed line) and ALDA (red solid line) calculations predict an energy onset for the excitation of $3p$ electrons in Cr that is too large, which should be a consequence of the failure of the LDA to describe the bonding energies of the semicore KS states for this material.

The d -to- d low-energy peak that is visible at ~ 4 eV in Fig. 8 is absent for small wave vectors and is therefore expected to have a very strong wave-vector dependence. Hence, in Fig. 9 we have illustrated this wave-vector dependence by plotting our full ALDA calculations (lines) and IXS measurements (circles) of the dynamical structure factor $s(\mathbf{q}, \omega)$ of Cr at wave vectors of magnitude ranging from ~ 0.7 to 3.5 \AA^{-1} along the (100) and (111)

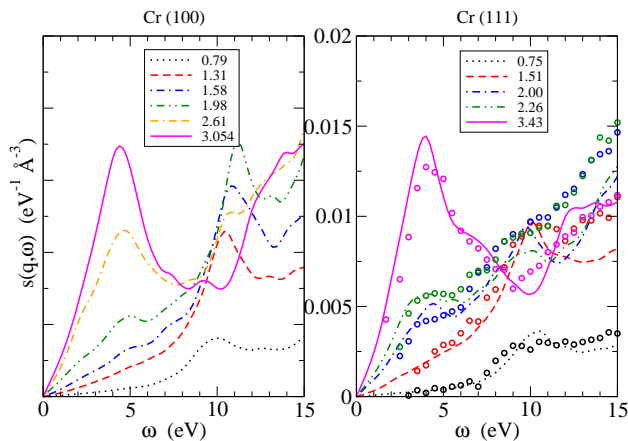


FIG. 9: (Color online) Formation of the $d \rightarrow d$ transition peak along the (100) and (111) directions, for different values of the wave vector (shown in \AA^{-1}).

directions (left and right panels, respectively). First, we note that both theory and experiment indicate that the weight of the d -to- d low-energy peak at ~ 4 eV, which is absent for small wave vectors, considerably increases with \mathbf{q} . Secondly, it is clear from this figure that ALDA calculations of this low-energy feature are in remarkable agreement with experiment for *all* wave vectors and prove

not only the presence of considerable crystal local-field effects below the M-edge but also the importance of IXS for the examination of the electronic structure of a $3d$ transition metal such as Cr.

Finally, we note that the d -to- d low-energy peak that is visible at ~ 4 eV in Figs. 4 and 8 is considerably sharper and more intense in the case of Cr (Fig. 8) than in the case of Sc (Fig. 4). This is simply due to the fact that in the case of Cr the density of d states is considerably large not only above the Fermi level but also below, thus increasing the number of available d -to- d transitions.

C. The $3d$ series

As we move along the $3d$ transition-metal period, from Sc to Ni, the $3d$ shell fills up causing a shift of the $3d$ bands towards the occupied side of the band structure below the Fermi level, as illustrated by the density of states that have been plotted in Fig. 10. Here we focus on the impact that this filling up of the $3d$ bands has on the collective excitations that are present for small wave vectors and, more importantly, on the *new* low-energy feature that is originated in the building up of d -to- d transitions.

	Sc	Ti	V	Cr	Fe	Co	Ni
Electronic structure [Ar]	$3d^1 4s^2$	$3d^2 4s^2$	$3d^3 4s^2$	$3d^5 4s^1$	$3d^6 4s^2$	$3d^7 4s^2$	$3d^8 4s^2$
Crystal structure	hcp	hcp	bcc	bcc	bcc	hcp	fcc
Points in IBZ	90	90	47	47	47	90	72
low \mathbf{q} (\AA^{-1})	0.44	0.42	0.41	0.43	0.44	0.37	0.29
large \mathbf{q} (\AA^{-1})	2.98	3.01	2.91	3.05	3.06	2.99	3.27

TABLE I: Parameters used for the comparative study of the $3d$ transition metals. Low \mathbf{q} and large \mathbf{q} refer to the magnitude of the wave vector used in Figs. 11 and 12, respectively.

1. Collective excitations

Full ALDA calculations of the dynamical structure factor $s(\mathbf{q}, \omega)$ of $3d$ transition metals are depicted in Fig. 11 at a low wave vector of magnitude $\sim 0.4 \text{\AA}^{-1}$ along the (001) direction and for energies below the M-edge. This figure clearly shows that in the case of $3d$ metals with five or fewer d states occupied per atom (Sc, Ti, V, and Cr) a broad peak can be identified, which mixes with the fine structure due to d -electron transitions. As the $3d$ band fills up (Fe, Co, and Ni), however, the number of states available for real transitions from occupied d bands below to unoccupied p states above the Fermi level considerably increases. Furthermore, the combination of

band-structure effects and the building-up of collective modes of d electrons yields broader structures in these materials which may still be in the nature of collective excitations but which are not well defined any more.

We note in passing that our first-principles calculations are in good agreement with the IXS measurements of the dynamical structure factor of Ti reported by Macrander *et al.*²⁵

2. $d \rightarrow d$ transitions

Figure 12 shows full ALDA calculations of the dynamical structure factor $s(\mathbf{q}, \omega)$ of the $3d$ transition metals Sc,

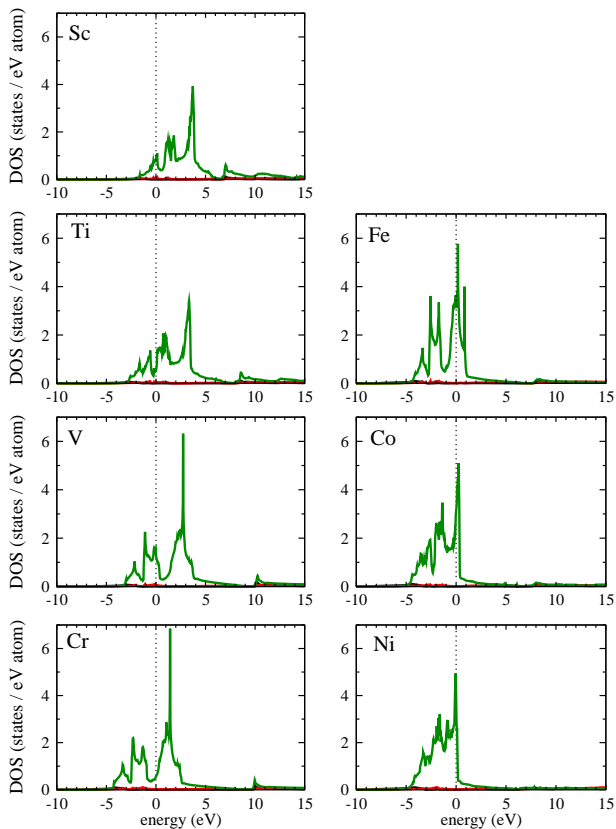


FIG. 10: (Color online) d content of the density of states in the $3d$ transition metal row, as we move from Sc to Ni (in the figure from top to bottom and left to right).

Ti, V, Cr, Fe, Co, and Ni and the corresponding IXS measurements for the $3d$ transition metals Sc (green circles) and Cr (blue squares) at a large wave vector of magnitude $|\mathbf{q}| \sim 3 \text{ \AA}^{-1}$ and low energies well below the M-edge. This figure clearly shows the presence of a low-energy peak at $\sim 4 \text{ eV}$, which follows the trends of the density of states depicted in Fig. 10 as should be expected from a feature that is originated in the building up of d -to- d transitions involving narrow d complexes lying below and above the Fermi level. The weight of this characteristic peak is small in Sc, which holds one single occupied d state per atom, it considerably increases in the case of Ti and V, as more d states become occupied, and it is extremely well defined in the case of Cr, with a half-filled $3d$ band below the Fermi level. As still more d states become occupied, as occurs in the case of Fe and Co, the number of states available for real transitions involving d -to- d transitions decreases again, thereby decreasing the weight of the $\sim 4 \text{ eV}$ peak. Finally, in the case of Ni, with only two unoccupied $3d$ states per atom, this feature is hardly visible.

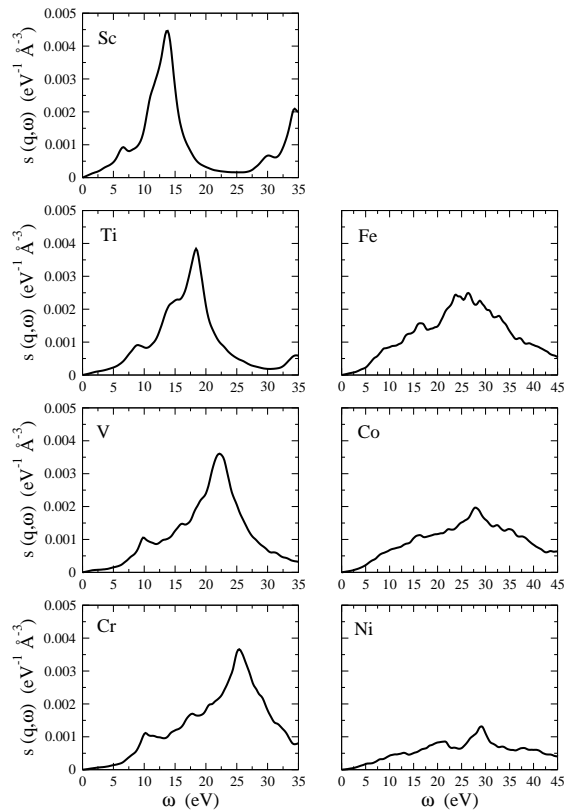


FIG. 11: Dynamical structure factor of the $3d$ transition metals along the (001) direction for a similar magnitude of the momentum transfer ($|\mathbf{q}| \sim 0.4 \text{ \AA}^{-1}$) and energies below the M-edge. The exact value of the momentum transfer can be found in Table I.

V. SUMMARY AND CONCLUSIONS

We have presented a combined theoretical and experimental investigation of the dynamical structure factor of various $3d$ transition metals with d states below and above the Fermi level. Calculations have been carried out for Sc, Ti, V, Cr, Fe, Co, and Ni by first expanding single-particle Bloch states in an LAPW basis and then computing the density-response function of the solid either in the RPA or the ALDA with full inclusion of crystal local-field effects. The experimental dynamical structure factor has been obtained for Sc and Cr by first performing nonresonant IXS measurements of the relative intensity of the scattered beam at a given wave vector and energy and then reducing the measured spectra to absolute units from sum-rule considerations.

For small wave vectors, a collective excitation of hybridized $3d$ and $4s$ electrons is observed, which is very well described by our ALDA calculations and which in the case of $3d$ metals holding five or fewer d states per atom (Sc, Ti, V, and Cr) has a rather well defined energy. At large wave vectors, IXS measurements exhibit a *new* feature at $\sim 4 \text{ eV}$, which (i) had never been observed before, (ii) we have found to be originated in the presence

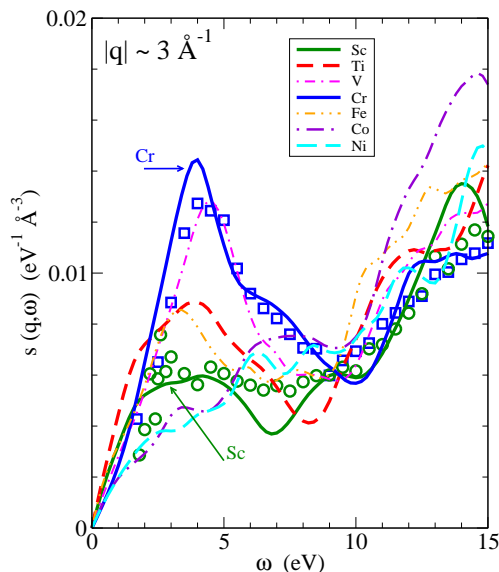


FIG. 12: (Color online) Low energy peak arising from $d \rightarrow d$ transitions for a large wave vector, as we move from left (Sc) to right (Ni) along the $3d$ row. The magnitude of the momentum transfer for each metal can be found in Table I. Lines denote the *ab initio* ALDA calculations and circles and squares correspond to the normalized IXS measurements on Sc and Cr, respectively.

of d -to- d transitions involving d states below and above the Fermi level, and (iii) is remarkably well described by our ALDA calculations, as long as crystal local-field effects are fully included. This new feature is absent at the small wave vectors accessible by EELS, and underscores the importance of IXS for investigations of the electronic structure and the dynamical response of transition metals.

Our ALDA calculations and IXS measurements of the dynamical structure factor of the transition metals Sc and Cr have been found to show a remarkable agreement at energies below the M-edge. However, at energies

above the M-edge significant discrepancies are found to exist between theory and experiment. Discrepancies between theory and experiment at the onset of the semicore excitations in Cr provide a signature of the single-particle LDA energies underestimating the binding energy of the semicore states. Discrepancies at the intensity and overall shape of the edge, especially in the case of Sc, should be due to the fact that the adiabatic local-density approximation for the many-body kernel breaks down at these large energies. These discrepancies call for further investigations of the accuracy of various approximations for the XC kernel of TDDFT.

Acknowledgments

I.G.G. and J.M.P. acknowledge partial support by the UPV/EHU, the Basque Unibertsitate, Hezkuntza eta Ikerketa Saila, the MCyT, and the EC 6th framework Network of Excellence NANOQUANTA (NMP4-CT-2004-500198). W.K. acknowledges support from the U.S. DOE under Contract No. DE-AC02-98CH10886. A.G.E. acknowledges support from NSF ITR DMR-0219332. K.D.F. acknowledges support by the National Science Foundation and the National Institutes of Health under award DMR-0225180. ORNL research sponsored by the DOE, Office of Science, DMS under contract with UT-Battelle, LLC. The UNICAT facility at the Advanced Photon Source (APS) is supported by the U.S. DOE under Award No. DEFG02-91ER45439, through the Frederick Seitz Materials Research Laboratory at the University of Illinois at Urbana-Champaign, the Oak Ridge National Laboratory (U.S. DOE contract DE-AC05-00OR22725 with UT-Battelle LLC), the National Institute of Standards and Technology (U.S. Department of Commerce) and UOP LLC. The APS is supported by the U.S. DOE, Basic Energy Sciences, Office of Science under contract No. W-31-109-ENG-38. I.G.G. gratefully acknowledges the hospitality of the University of Tennessee, Knoxville, and Oak Ridge National Laboratory, where most of these calculations were carried out.

¹ D. Pines and P. Nozières, *The Theory of Quantum Liquids* (W. A. Benjamin, Inc, New York, 1966).

² A. A. Quong and A. G. Eguiluz, Phys. Rev. Lett. **70**, 3955 (1993).

³ F. Aryasetiawan and K. Karlsson, Phys. Rev. Lett. **73**, 1679 (1994).

⁴ N. E. Maddocks, R. W. Godby, and R. J. Needs, Europhys. Lett. **27**, 681 (1994).

⁵ A. Fleszar, A. A. Quong, and A. G. Eguiluz, Phys. Rev. Lett. **74**, 590 (1995).

⁶ A. Fleszar, R. Stumpf, and A. G. Eguiluz, Phys. Rev. B **55**, 2068 (1997).

⁷ M. Rohlfing and S. G. Louie, Phys. Rev. B **62**, 4927 (2000).

⁸ I. Campillo, A. Rubio, and J. M. Pitarke, Phys. Rev. B **59**, 12188 (1999).

⁹ M. A. Cazalilla, J. S. Dolado, A. Rubio, and P. M. Echenique, Phys. Rev. B **61**, 8033 (2000).

¹⁰ I. G. Gurtubay, J. M. Pitarke, I. Campillo, and A. Rubio, Comp. Mater. Sci. **22**, 123 (2001).

¹¹ W. D. Schöne and W. Ekaradt, J. Phys.: Condens. Matter **14**, 4669 (2002).

¹² I. G. Gurtubay, W. Ku, J. M. Pitarke, and A. G. Eguiluz, Comp. Mater. Sci. **30**, 104 (2004).

¹³ N. Vast, L. Reining, V. Olevano, P. Schattschneider, and B. Jouffrey, Phys. Rev. Lett. **88**, 037601 (2002).

¹⁴ I. G. Gurtubay, W. Ku, J. M. Pitarke, A. G. Eguiluz, B. C. Larson, J. Z. Tischler, and P. Zschack, Phys. Rev. B **70**, 201201(R) (2004).

¹⁵ A. G. Eguiluz, O. D. Restrepo, B. C. Larson, J. Z. Tischler, P. Zschack, and G. E. Jellison (2005), submitted to J. Phys.

- Chem. Solids.
- ¹⁶ W. Ku, W. E. Pickett, R. T. Scalettar, and A. G. Eguiluz, *Phys. Rev. Lett.* **88**, 057001 (2002).
 - ¹⁷ S. Grenier, J. P. Hill, V. Kiryukhin, W. Ku, Y.-J. Kim, K. J. Thomas, S.-W. Cheong, Y. Tokura, Y. Tomioka, D. Casa, et al., *Phys. Rev. Lett.* **94**, 047203 (2005).
 - ¹⁸ S. L. Adler, *Phys. Rev.* **126**, 413 (1962).
 - ¹⁹ H. Raether, *Excitation of Plasmons and Interband Transitions by Electrons*, vol. 88 of *Springer Tracts in Modern Physics* (Springer-Verlag, Berlin, 1980).
 - ²⁰ D. L. Misell and A. J. Atkins, *Philos. Mag.* **27**, 95 (1973).
 - ²¹ P. Eisenberger, P. M. Platzman, and C. Pandey, *Phys. Rev. Lett.* **31**, 311 (1973).
 - ²² P. M. Platzman, E. D. Isaacs, H. Williams, P. Zschack, and G. E. Ice, *Phys. Rev. B* **46**, 12943 (1992).
 - ²³ W. Schülke, J. R. Schmitz, H. Schulte-Screpping, and A. Kaprolat, *Phys. Rev. B* **52**, 11721 (1995).
 - ²⁴ B. C. Larson, J. Z. Tischler, E. D. Isaacs, P. Zschack, A. Fleszar, and A. G. Eguiluz, *Phys. Rev. Lett.* **77**, 1346 (1996).
 - ²⁵ A. T. Macrander, P. A. Montano, D. L. Price, V. I. Kushnir, R. C. Blasdel, C. C. Kao, and B. R. Cooper, *Phys. Rev. B* **54**, 305 (1996).
 - ²⁶ P. A. Montano, D. L. Price, A. T. Macrander, and B. R. Cooper, *Phys. Rev. B* **66**, 165218 (2002).
 - ²⁷ W. Kohn and L. Sham, *Phys. Rev.* **140**, A11333 (1965).
 - ²⁸ R. M. Dreizler and E. K. U. Gross, *Density Functional Theory* (Springer-Verlag, Berlin, 1990).
 - ²⁹ D. Singh, *Pseudopotentials and the LAPW Method* (Kluwer Academic Publishers, Boston, Dordrecht, London, 1994).
 - ³⁰ P. Blaha, K. Schwarz, and J. Luitz, *WIEN97, A Full Potential Linearized Augmented Plane Wave Package for Calculating Crystal Properties*, Technische Universität Wien, Austria (1999), ISBN 3-9501031-0-4.
 - ³¹ W. Ku, Ph.D. thesis, The University of Tennessee, Knoxville (2000).
 - ³² E. Runge and E. K. U. Gross, *Phys. Rev. Lett.* **52**, 997 (1984).
 - ³³ E. K. U. Gross and W. Kohn, *Phys. Rev. Lett.* **55**, 2850 (1985).
 - ³⁴ M. Petersilka, U. J. Gossmann, and E. K. U. Gross, *Phys. Rev. Lett.* **76**, 1212 (1996).
 - ³⁵ H. B. Callen and T. R. Welton, *Phys. Rev.* **83**, 34 (1951).
 - ³⁶ J. Z. Tischler, B. C. Larson, P. Zschack, A. Fleszar, and A. G. Eguiluz, *Phys. Stat. Sol. (b)* **237**, 280 (2003).
 - ³⁷ J. P. Perdew and Y. Wang, *Phys. Rev. B* **45**, 13244 (1992).
 - ³⁸ D. M. Ceperley and B. J. Alder, *Phys. Rev. Lett.* **45**, 566 (1980).
 - ³⁹ B. Brousseau-Lahaye, C. Colliex, J. Frandon, M. Gasgnier, and P. Trebbia, *Phys. Stat. Sol. (b)* **69**, 257 (1975).
 - ⁴⁰ P. A. Montano and A. T. Macrander, *J. Phys. Chem. Solids* **61**, 415 (2000).
 - ⁴¹ The density-response function of a many-electron system yields the electron density induced at a given point of space by an arbitrary (small) frequency-dependent external potential.
 - ⁴² The actual number of \mathbf{G} vectors needed for convergence depends on the spectral feature. While the semicore is the feature which needs the largest numbers, fewer \mathbf{G} vectors are required in the valence region.
 - ⁴³ The electron density n_0 of a homogeneous electron gas is typically characterized by the density parameter $r_s = (3/4\pi n_0)^{1/3}/a_0$, a_0 being the Bohr radius.
 - ⁴⁴ This deficiency contributes to the discrepancy between ALDA calculations and experiment; however, the *large* discrepancies that are visible in Figs. 3 and 4 should be searched in the adiabaticity and the locality of the ALDA XC kernel.
 - ⁴⁵ We have carried out RPA calculations and IXS measurements of the dynamical structure factor of Al, and we have found that the LDA predicts the $2p$ semicore states of this material to be located at ~ 65 eV while the IXS measurements show the $2p$ semicore excitation onset at ~ 72 eV.
 - ⁴⁶ At the wave vectors and energies under consideration crystal local-field effects in Cr are small and one finds, therefore, $\epsilon_M(\mathbf{q}, \omega) \approx \epsilon_{0,0}(\mathbf{q}, \omega)$.
 - ⁴⁷ In order to be able to choose similar values of the magnitude of the momentum transfer along the three directions under study, we have used two different samplings of the BZ, $10 \times 10 \times 10$ and $11 \times 11 \times 11$. As the damping parameter η has been taken to be $\eta = 0.65$ eV in both cases, small differences among the three curves may be due not only to the fact that the magnitude of the wave vector is not exactly the same but also to the fact that different samplings of the BZ have been used with the same value of η .